Tensor Data Conformity Evaluation for Interference-Resistant Localization

Konstantinos Tountas*, George Sklivanitis*, Dimitris A. Pados*, Michael J. Medley‡
*I-SENSE and Department of Electrical and Computer Engineering and Computer Science
Florida Atlantic University, Boca Raton, FL 33431
E-mail: {ktountas2017, gsklivanitis, dpados}@fau.edu
‡US Air Force Research Laboratory, Rome, NY 13440
E-mail: michael.medley@us.af.mil

ABSTRACT

We consider the problem of robust, interference-resistant localization in GPS-denied environments. Each asset to be self-localized is equipped with an antenna array and leverages time-domain coded beacon signals from anchor nodes that are placed at known locations. Collected data snapshots over time at the antenna array are organized in a tensor data structure. The conformity of the received tensor data is evaluated through iterative projections on robust, high-confidence data feature characterizations that are returned by L1-norm tensor subspaces. Non-conforming tensor slabs are more likely to be contaminated by irregular, highly deviating measurements due to interference, thus they are removed from the received dataset. Subsequently, we estimate the direction-of-arrival of the beacon signals by using L2-norm and L1-norm tensor decomposition techniques on the conformity-adjusted dataset. Finally, the relative position of the asset to the anchor nodes is estimated via triangulation. We consider two anchor nodes, one interferer, and one asset to be self-localized using radio frequency signals at the 2.4 GHz ISM band in an indoor laboratory environment. We evaluate the performance of the proposed localization system in terms of angle-of-arrival estimation accuracy experimental measurements from a software-defined radio testbed.

I. INTRODUCTION

Autonomous Unmanned vehicles (AUVs) have attracted considerable attention for military, scientific and industrial applications including search and rescue [1], [2], industrial inspection [3], [4], precision agriculture [5] and monitoring remote environments [6]. Nearly all applications require precise latitude and longitude estimates of the UAV during operation. This level of localization may not be available in GPS-denied and requires the use of often costly GPS hardware and IMUs. Self-localization of AUVs relatively to known location GPS-assisted beacons or other vehicles in swarm deployment can help the vehicle navigate in the environment, reliably communicate and network with other vehicles and stamp collected sensor data with a spatial reference.

GPS-free localization schemes proposed for terrestrial radio networks involve intensive message exchanges and therefore are not suitable for deployments with low-bandwidth, high-latency radios. Typical wireless localization techniques rely on angle or distance measurements between wirelessly communicating nodes that are collected by received-signal-strength (RSS), time-of-arrival (ToA), time-of-flight (ToF), time-difference-of-arrival (TDoA), and angle-of-arrival (AoA) techniques [7]. Authors in [8] propose an ESPRIT-based angle-of-arrival estimation method based on the L2-norm higher-order singular value decomposition (HOSVD) for calculating the underlying signal subspaces. In [9] a bearing-only localization method was presented along with an approximation algorithm with a constant factor performance guarantees. [10] demonstrates how an agent is able to localize a stationary target using bearing-only measurements. State-of-the-art works utilize the simultaneous localization and mapping (SLAM) method, which is well described in [11], [12]. SLAM algorithms are used to develop landmark-based navigation systems with the capability of online building mapping. Authors in [13] presented the integration of vision-based measurements with inertial navigation systems to simultaneously localize an UAV through the position of some extracted features by image processing. The above localization techniques offer good accuracy under nominal operation conditions. However, their performance significantly degrades in the presence of outlier measurements due to intermittent environmental disturbances, and hardware and/or channel impairments (such as channel path variations, impulsive noise sources, and faulty measurements).

Existing approaches for subspace-based parameter estimation [14], [15] rely on organization of the collected data snapshots at the receiver array in matrices by means of the stacking operation. Matrix representation does not account for the structure that is inherent in the wireless channel data recordings. A more natural approach to store and manipulate multidimensional data is given by tensors. In this paper, we show that the tensor representation allows us to fully exploit the structure of space-time coded data as these arrive at the input of an antenna array. More specifically, we consider the deployment of an autonomous unmanned vehicle that is equipped with a D-element antenna array. The AUV can robustly self-localize by accurately estimating the azimuth and

The work of K. Tountas, G. Sklivanitis and D. A. Pados was supported by the National Science Foundation, under grant CNS-1753406. The work of D. A. Pados was also supported by the Schmidt Family Foundation.
The views and conclusions contained herein are those of the authors and should not be interpreted as necessarily representing the official policies or endorsements, either expressed or implied, of the Air Force Research Laboratory or the U.S. Government.

elevation angles-of-arrival of reference transmitted beacons. The beacons are single-antenna nodes that are deployed in known locations and transmit time-domain coded signals in a spread-spectrum fashion. Orthogonal codes of length L enable simultaneous beacon transmissions in frequency and time. We consider that all transmitted signals propagate over multi-path fading channels in the presence of intermittent interference. The received signals at the input of the antenna array are then organized in a tensor structure. We show that by employing data conformity evaluation [16] we can clean the received tensor and remove slabs corrupted by interference, thus offering superior angle-of-arrival (AoA) estimation and positioning accuracy. We demonstrate the effectiveness of our proposed data cleaning technique on experimental measurements from a software-defined radio testbed.

II. System Model

We consider information symbol transmissions of K asynchronous single-antenna beacons over a single-input multiple-output (SIMO) flat fading channel with M resolvable propagation paths as depicted in Fig. 1. The transmitted signal of the k-th beacon is written as

$$x_k(t) = \sqrt{E_k} \sum_n b_k[n] s_k(t - nT) e^{j(2\pi f_c t + \phi_k)} \tag{1}$$

where ϕ_k is the carrier phase, f_c is the carrier center frequency and the n-th symbol for the k-th beacon $b_k[n]$ is drawn from a complex constellation $\mathcal{C}$ of energy $E_k > 0$, and modulated by an all-spectrum digital waveform $s_k(t)$ that is given by

$$s_k(t) = \sum_{l=0}^{L-1} \mathbf{d}_k[l] g_{T_c}(t - lT_c) \tag{2}$$

where $\mathbf{d}_k \in \left\{ \pm \frac{1}{\sqrt{L}} \right\}^L$ is a binary code of length L, and $g_{T_c}(\cdot)$ is a square-root raised cosine (SRRC) pulse with roll-off factor α and duration T_c, so that $T = LT_c$.

The transmitted signals propagate over Rayleigh fading multipath channels with M resolvable paths and experience additive Gaussian noise at the receiver. Multipath fading is modeled by a liner tapped-delay line with taps that are spaced at T_c intervals and are weighted by independent fading coefficients (i.e. Rayleigh distributed amplitude and uniformly distributed phase).

The signals are received by an antenna array with D elements. As a result, the array response vector $\mathbf{a}(\phi_k, \theta_k), k = 1, \ldots, K$ to a far-field received signal that impinges on the array at an azimuth angle ϕ_k and an elevation angle θ_k, is given by

$$\mathbf{a}(\phi_k, \theta_k) = \exp\left\{ j2\pi \frac{1}{\lambda_c} \mathbf{P}^T \mathbf{v}(\phi_k, \theta_k) \right\} \in \mathbb{C}^{D \times 1} \tag{3}$$

where λ_c is the carrier wavelength, $\mathbf{P}$ includes the antenna array element positions

$$\mathbf{P} = \begin{bmatrix} x_1 & x_2 & \ldots & x_D \\ y_1 & y_2 & \ldots & y_D \\ z_1 & z_2 & \ldots & z_D \end{bmatrix} \in \mathbb{R}^{3 \times D} \tag{4}$$

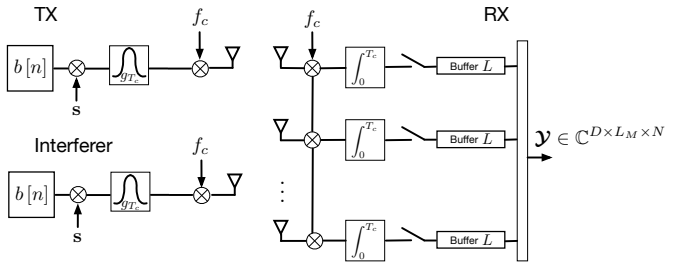

Fig. 1: System model of the D antenna-element direction-of-arrival estimation system.

and $\mathbf{v}(\phi_k, \theta_k)$ represents the projection of the received signal's steering vector on the antenna array coordinate system that is defined as

$$\mathbf{v}(\phi_k, \theta_k) = \begin{bmatrix} \cos(\theta_k)\sin(\phi_k) \\ \cos(\theta_k)\cos(\phi_k) \\ \sin(\theta_k) \end{bmatrix} \in \mathbb{R}^{3 \times 1}. \tag{5}$$

The carrier demodulated and pulse-matched filtered received signal vector after sampling over the symbol duration and buffering $L_M = L + M - 1$ samples, the n-th received space-code data snapshot matrix $\mathbf{Y}_n \in \mathbb{C}^{D \times L_M}$ is written as

$$\mathbf{Y}_n = \sum_{k=1}^{K} \sqrt{E_k} b_k[n] \, \mathbf{a}(\phi_k, \theta_k) \left(\mathbf{H}_k \mathbf{d}_k \right)^T + \mathbf{I}_n + \mathbf{N}_n, \tag{6}$$

where $\mathbf{H}_k \in \mathbb{C}^{L_M \times L}$ denotes the multipath channel matrix of the k-th beacon defined as

$$\mathbf{H}_k \triangleq \begin{bmatrix} h_{k,1} & 0 & \cdots & 0 \\ h_{k,2} & h_{k,1} & \cdots & 0 \\ \vdots & \vdots & \cdots & \vdots \\ h_{k,M} & h_{k,M-1} & \cdots & 0 \\ 0 & h_{k,M} & \cdots & h_{k,1} \\ \vdots & \vdots & \cdots & \vdots \\ 0 & 0 & \cdots & h_{k,M} \end{bmatrix}, \tag{7}$$

where $h_{k,m}, m = 1, 2, \ldots, M$ is considered an independent zero-mean complex Gaussian random variable that models the m-th complex baseband channel coefficient for the k-th beacon. $\mathbf{I}_n \in \mathbb{C}^{D \times L_M}$ models colored interference at the receiver array and $\mathbf{N}_n \in \mathbb{C}^{D \times L_M}$ models zero-mean additive white Gaussian noise with autocorrelation matrix $\mathbf{R}_n \triangleq \mathbb{E}\left\{ \mathbf{N}\mathbf{N}^H \right\} = \sigma^2 \mathbf{I}_D$.

By defining the power-scaled, channel-processed signature matrix $\mathbf{S} = [\mathbf{s}_1, \ldots, \mathbf{s}_K] \in \mathbb{C}^{L_M \times K}$, where $\mathbf{s}_k = \sqrt{E_k}\mathbf{H}_k\mathbf{d}_k \in \mathbb{C}^{L_M \times 1}$, the rank-$D$ steering matrix $\mathbf{A} = [\mathbf{a}(\phi_1, \theta_1), \ldots, \mathbf{a}(\phi_K, \theta_K)] \in \mathbb{C}^{D \times K}$, and a diagonal matrix $\mathbf{B}[n] = diag([b_1[n], b_2[n], \ldots, b_K[n]])$, the n-th received data snapshot matrix in (6) can be expressed in matrix form as

$$\mathbf{Y}_n = \mathbf{A}\mathbf{B}_n\mathbf{S}^T + \mathbf{I}_n + \mathbf{N}_n \in \mathbb{C}^{D \times L_M}. \tag{8}$$

We observe that the received matrices can be viewed as slices of a three-way tensor $\boldsymbol{\mathcal{Y}}_C \in \mathbb{C}^{D \times L_M \times N}$. Some of the N slabs are going to be corrupted by colored interference. Our goal is to evaluate the conformity of each slab of the received

tensor $\boldsymbol{\mathcal{Y}}$ and remove the slabs that are more likely to be contaminated by irregular, highly deviating measurements due to interference.

In order to continue our algorithmic developments, we define the real-valued representation $\bar{\mathbf{A}} \in \mathbb{R}^{2m\times 2n}$ of any complex-valued matrix $\mathbf{A} \in \mathbb{C}^{m\times n}$ by concatenating real and imaginary parts as follows

$$\bar{\mathbf{A}} = \begin{bmatrix} \mathrm{Re}\{\mathbf{A}\} & -\mathrm{Im}\{\mathbf{A}\} \\ \mathrm{Im}\{\mathbf{A}\} & \mathrm{Re}\{\mathbf{A}\} \end{bmatrix}, \tag{9}$$

where $\mathrm{Re}\{\cdot\}$ and $\mathrm{Im}\{\cdot\}$ return the real and imaginary part of each matrix element, respectively. The transition from $\mathbf{A} \in \mathbb{C}^{m\times n}$ to $\bar{\mathbf{A}} \in \mathbb{R}^{2m\times 2n}$ is based on what is commonly referred to as complex-number realification in representation theory. Realification allows for any complex system of equations to be converted and solved through a real system.

With the realification operation, we convert our complex tensor $\boldsymbol{\mathcal{Y}} \in \mathbb{C}^{D\times L_M\times N}$ to a real-valued tensor $\bar{\boldsymbol{\mathcal{Y}}} \in \mathbb{R}^{2D\times 2L_M\times 2N}$

III. Data Conformity Evaluation

Data conformity evaluation converts the original tensor data to a new tensor of the exact same dimensions, where each new tensor entry measures the conformity of that entry with respect to all other data points. The conformity metric will take values from the $[0, 1]$ set of real numbers, with conformity values close to 1 indicating "misbehaving" data points, and values close to 0 corresponding to nominal data points. This is achieved, by utilizing iteratively refined L_1-norm (absolute-error) data subspaces [15], [17], [18]. Detection of non-conforming data entries enables the identification of contaminated received slabs.

L_1-norm principal component analysis (PCA), is by itself a fundamental data feature learning approach that is arguably best suited for robust, high-confidence characterization and identification of faulty data patterns [19]. Data conformity evaluation of tensor data was proposed for outlier identification in [16]. Without loss of generality, we describe the steps of the tensor conformity evaluation algorithm with respect to the column unfolding of the tensor $\bar{\mathbf{Y}}_{(1)} \in \mathbb{R}^{2D\times 4L_MN}$.

Unfolding along the columns of the tensor we calculate the $1 \le r_1 \le (4L_MN)$ principal components $\mathbf{Q}_1^{(0)} \in \mathbb{R}^{2D\times r_1}$ by solving the following maximization problem [17], [18]

$$\mathbf{Q}_1^{(0)} = \underset{\substack{\mathbf{Q}\in\mathbb{R}^{2D\times r_1},\\ \mathbf{Q}^T\mathbf{Q}=\mathbf{I}_{r_1}}}{\mathrm{argmax}} \left\| \bar{\mathbf{Y}}_{(1)}^T \mathbf{Q} \right\|_1. \tag{10}$$

The resulting basis describes accurately the subspace spanned by the columns of the original tensor $\boldsymbol{\mathcal{Y}}$ that contain nominal data. Columns that are contaminated with anomalous data are not spanned by the resulting basis vectors. The conformity of the data columns is computed by projecting each column $\left[\bar{\mathbf{Y}}_{(1)}\right]_{:,i_1}, i_1 = 1, 2, \ldots, 4L_MN$ on the calculated subspace $\mathbf{Q}_1^{(0)}$ as

$$d_{1,i_1}^{(1)} = \left\| \mathbf{Q}_1^{(0)} \mathbf{Q}_1^{(0)^T} \left[\bar{\mathbf{Y}}_{(1)}\right]_{:,i_1} \right\|_2^{-1} \quad \forall i_1 = 1, 2, \ldots, 4L_MN. \tag{11}$$

Algorithm 1 Data Cleaning and Angle-of-Arrival Estimation through Data Conformity Evaluation

Input: $\boldsymbol{\mathcal{Y}} \in \mathbb{C}^{D\times L_M\times N}$; ranks r_1, r_2, r_3; weights $\alpha_1, \alpha_2, \alpha_3$
Output: angles-of-arrival $\phi_k, \theta_k, k = 1, 2, \ldots, K$

1: Calculate $\bar{\boldsymbol{\mathcal{Y}}} \leftarrow$ realification $(\boldsymbol{\mathcal{Y}})$ according to Eq. (9)
2: Calculate $\bar{\boldsymbol{\mathcal{W}}} \leftarrow DataConformityEvaluation\left(\bar{\boldsymbol{\mathcal{Y}}}\right)$
3: Calculate $\bar{\mathbf{w}} \in [0, 1]^{N\times 1}$ according to (14).
4: Calculate $\boldsymbol{\mathcal{Y}}'$ by removing slabs from $\bar{\boldsymbol{\mathcal{Y}}}$ with mean conformity $\bar{w}_n$ less than the threshold t_{corr}.
5: Calculate $\mathbf{Q}_{\mathrm{SC}} \leftarrow \mathrm{SVD}\left(\mathrm{vec}\left(\boldsymbol{\mathcal{Y}}'\right)\right)$
6: Find the K maximum peaks of P_{SC} according to (16).

Function: Data Conformity Evaluation Algorithm [16]

Input: $\boldsymbol{\mathcal{X}} \in \mathbb{C}^{I_1\times I_2\times I_3}$; ranks $r_1, r_2, r_3 \in \mathbb{Z}^+$; weights $\alpha_1, \alpha_2, \alpha_3$
Output: $\boldsymbol{\mathcal{W}} \in \mathbb{R}^{I_1\times I_2\times I_3}$

for k = 1, 2, 3 **do**
  $\mathbf{Q}_k^{(0)} = \underset{\substack{\mathbf{Q}\in\mathbb{R}^{I_k\times r_k},\\ \mathbf{Q}^T\mathbf{Q}=\mathbf{I}_{r_k}}}{\mathrm{argmax}} \left\| \mathbf{X}_{(k)}^T \mathbf{Q} \right\|_1$
  $M_k = \prod_{i=1, i\neq k}^{3} I_i$; $l = 1$
end for
while convergence criterion is not met **do**
  for $k = 1, 2, 3$ **do**
    $d_{k,i_k}^{(l)} = \left\| \mathbf{Q}_k^{(l-1)} \mathbf{Q}_k^{(l-1)^T} \left[\mathbf{X}_{(k)}\right]_{:,i_k} \right\|_2, \quad \forall i_k = 1, 2, \ldots, M_k$
    $\mathbf{D} = \left[d_{k,1}^{(l)} \quad \ldots \quad d_{k,M_k}^{(l)} \right]_{M_k\times 1}^{T} \odot \mathbf{1}_{M_k\times I_k}$
    $\boldsymbol{\mathcal{W}}_k^{(l)} \leftarrow \mathrm{tensorization}\left(\mathbf{D}, k\right)$
  end for
  $\boldsymbol{\mathcal{W}}^{(l)} = \frac{\sum_{k=1}^{3} \alpha_k \boldsymbol{\mathcal{W}}_k^{(l)} - \min\left(\sum_{k=1}^{3} \alpha_k \boldsymbol{\mathcal{W}}_k^{(l)}\right)}{\max\left(\sum_{k=1}^{3} \alpha_k \boldsymbol{\mathcal{W}}_k^{(l)}\right) - \min\left(\sum_{k=1}^{3} \alpha_k \boldsymbol{\mathcal{W}}_k^{(l)}\right)}$
  for $k = 1, 2, 3$ **do**
    $\mathbf{Q}_k^{(l)} = \underset{\substack{\mathbf{Q}\in\mathbb{C}^{I_k\times r_k},\\ \mathbf{Q}^T\mathbf{Q}=\mathbf{I}_{r_k}}}{\mathrm{argmax}} \left\| \left(\mathbf{X}_{(k)} \circ \mathbf{W}_{(k)}^{(l)}\right)^T \mathbf{Q} \right\|_1$
  end for
  $l = l + 1$
end while

Large $d_{1,i_1}^{(1)}$ values are expected if $\left[\bar{\mathbf{Y}}_{(1)}\right]_{:,i_1}$ is an anomalous data vector and small $d_{1,i_1}^{(1)}$ values if $\left[\bar{\mathbf{Y}}_{(1)}\right]_{:,i_1}$ is a nominal data vector. After the calculation of the projection of each column on the subspace, the conformity values are converted to a tensor $\boldsymbol{\mathcal{W}}_1^{(1)} \in \mathbb{R}^{2D\times 2L_M\times 2N}$

$$\boldsymbol{\mathcal{W}}_1^{(1)} = \mathrm{tensorization}\left(\left[d_{1,1}^{(1)}, \ldots, d_{1,L_MN}^{(1)} \right]^T \odot \mathbf{1}_{2D\times 4L_MN}, 1 \right) \tag{12}$$

where $\mathbf{1}_{2D\times 4L_MN}$ stands for an all-ones matrix of dimension $2D \times 4L_MN$, and the *tensorization*$(\cdot)$ operation converts the first mode of the tensor to the original three mode tensor form (reverting the unfolding process). The tensor $\boldsymbol{\mathcal{W}}_1^{(1)}$ contains the conformity values corresponding to each column of the original tensor $\boldsymbol{\mathcal{Y}}$. We repeat the above process for the rest of the modes of the original data tensor, and calculate the

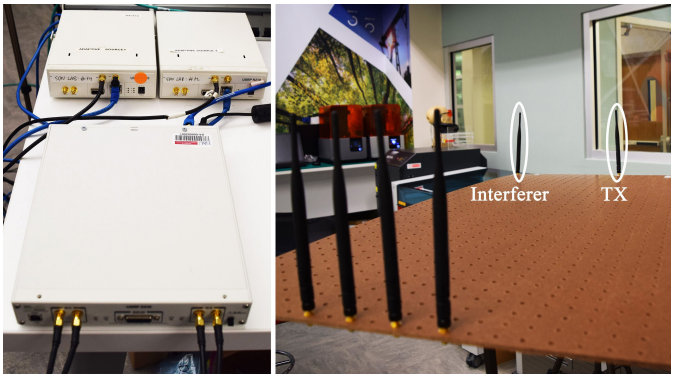

Fig. 3: Software-defined radio transmitters and receiver (left) and the topology of the testbed; the four antennas in the front are the ULA, while the two antennas in the back are the transmitter and the interferer.

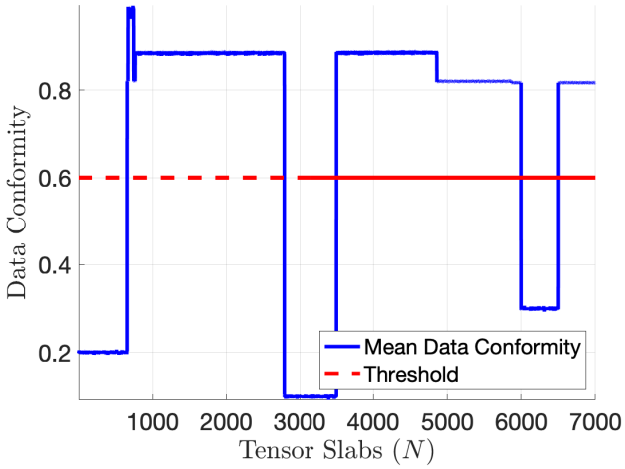

Fig. 4: Software-defined radio transmitters and receiver (left) and the topology of the testbed; the four antennas in the front are the ULA, while the two antennas in the back are the transmitter and the interferer.

conformity tensors $\boldsymbol{\mathcal{W}}_2^{(1)}$ and $\boldsymbol{\mathcal{W}}_3^{(1)}$. We calculate the final conformity tensor $\boldsymbol{\mathcal{W}}^{(1)}$ by combining the above calculated tensors in an additive fashion as well as normalizing the tensor so that each element is in the $[0, 1]$ range

$$\boldsymbol{\mathcal{W}}^{(1)} = \frac{\sum_{k=1}^{3} \alpha_k \boldsymbol{\mathcal{W}}_k^{(1)} - \min\left(\sum_{k=1}^{3} \alpha_k \boldsymbol{\mathcal{W}}_k^{(1)}\right)}{\max\left(\sum_{k=1}^{3} \alpha_k \boldsymbol{\mathcal{W}}_k^{(1)}\right) - \min\left(\sum_{k=1}^{3} \alpha_k \boldsymbol{\mathcal{W}}_k^{(1)}\right)} \tag{13}$$

where $\alpha_1, \alpha_2, \alpha_3 \in \mathbb{R}^+, \sum_{k=1}^{3} \alpha_k = 1$ correspond to weights for each mode of the tensor that model the weighting of the corresponding dimension of the original tensor. The final conformity tensor $\boldsymbol{\mathcal{W}}^{(1)}$ enables element-wise conformity of the original tensor data. The data conformity values can be iteratively refined until numerical convergence of the data conformity tensor $\boldsymbol{\mathcal{W}}^{(l)}$.

In order to identify slabs that are contaminated by interference, we calculate the mean data conformity value per slab as

$$\bar{w}_n = \frac{1}{4DL} \sum_{d=1}^{2D} \sum_{l=1}^{2L} [\boldsymbol{\mathcal{W}}]_{l,d,n}, n = 1, 2, \ldots, 2N. \tag{14}$$

Slabs with high conformity values contain contaminated data, while low-conformity slabs contain nominal data. We choose to remove slabs with conformity value $\bar{w}_n$ above a pre-defined threshold t_{cutoff} from the received tensor $\mathcal{Y}$, resulting in a new tensor $\mathcal{Y}' \in \mathbb{R}^{2D \times 2L_M \times N'}$, where $N' < 2N$. The new tensor $\mathcal{Y}'$ contains only slabs that are not contaminated by interference, which results in better estimation of the beacons' angles-of-arrival.

The next step in the localization process is the estimation of the beacons' angles-of-arrival. We utilize "MUSIC"-type AoA estimation by using the extended space-code search vector

$$\bar{\mathbf{z}}(\mathbf{d}, \phi, \theta) \triangleq \text{realify}(\mathbf{a}(\phi, \theta) \otimes \mathbf{d}) \in \mathbb{R}^{2DL_M \times 2}, \tag{15}$$

where the realification$(\cdot)$ operation realifies the input vector according to Eq. (9), $\mathbf{a}(\phi, \theta)$ is the antenna response vector given by (3), and $\mathbf{d} \in \{\pm 1\}^{L_M \times 1}$ corresponds to a binary waveform of length L. By vectorizing each tensor slab into a vector $\mathbf{y}'_n = \text{vec}(\mathbf{Y}'_n) \in \mathbb{R}^{4DL_M \times 1}$ and concatenating the resulting vectors, we create the data matrix $\mathbf{Y}' = [\mathbf{y}'_1, \mathbf{y}'_2, \ldots, \mathbf{y}'_{N'}]$. Then we calculate the rank r_{SC} signal subspace of $\mathbf{Y}'$, $\mathbf{Q}_{\text{SC}} \in \mathbb{C}^{4DL_M \times r_{\text{SC}}}$ by means of SVD and create the "MUSIC"-type spectrum

$$P_{\text{SC}}(\mathbf{d}, \phi, \theta) = \frac{1}{\left\|\mathbf{Q}_{\text{SC}} \mathbf{Q}_{\text{SC}}^H \mathbf{z}(\mathbf{d}, \phi, \theta)\right\|_2}. \tag{16}$$

The peak of $P_{\mathbf{d}_k,\text{SC}}(\phi, \theta)$ correspond to the angles-of-arrival of the k-th beacon. Algorithm **??** offers a complete description of the proposed data cleaning and angle-of-arrival estimation techniques.

IV. Performance Evaluation

We tested our algorithmic developments by conducting experiments on real data transmitted by one beacon in the presence of one sporadic interferer, gathered by a uniform-linear array (ULA). Our goal was to clear the received data and be able to clearly identify the AoA of the beacon. Our experimental setup consisted of two single antenna transmitters (one used by the beacon and one by the interferer) and $D = 4$ element ULA receiver. The antennas were placed on a 1.21×0.61 m pegboard and the distance between the transmit and the received antennas was 1.19 m. The distance between the beacon and the interferer was 0.3 m and the ULA antennas were placed $d = 0.2104$ m apart from each other. For the beacon and the interferer, we utilized two National Instruments USRPs N200 transmitting Binary-Phase-Shift-Keying (BPSK) symbols utilizing the same waveform $s(t)$ at 2.4 GHz carrier frequency. The transmitted signals were received by the ULA connected to a National Instruments USRP X310. With respect to the broadside of the ULA the beacon signal is received from an angle $\phi_1 = 0°$, while the interferer signal is received from an angle $\phi_2 = 15°$. Figure 3 depicts the experimental setup. Since a ULA is used on the receiver side, we can only identify the received azimuth angle ϕ, thus in the antenna response

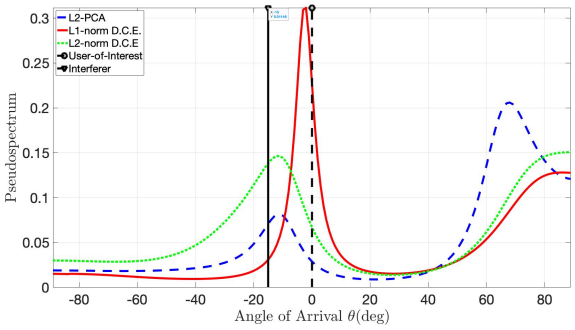

Fig. 5: Azimuth pseudo-spectrum of the received signal.

vector equation Eq. (3) we set $\theta = 0$. We run the data cleaning and conformity evaluation algorithm on the complex received data and calculate the conformity values of each slab. Fig. 4 depicts the per slab conformity values across $N = 7000$ tensor slabs. It is clearly shown that there are time instances were the received signal is highly non-conforming (conformity values close to 1).

After the removal the non-conforming slabs, we calculate the pseudo-spectrum P_{SC} according to Eq. (16) for $\theta = 0$. We compared against "MUSIC" L2-norm AoA estimation and state-of-the-art L2-norm based techniques (SVD) for calculation of the subspaces in the data conformity function (instead of L1-norm based). Fig. 5 depicts the AoA spectrum of the cleaned data set. The unclean L2-norm MUSIC and the L2-norm based data conformity cleaning clearly fail to identify the AoA of the beacon, and the spectrum is corrupted. The proposed L1-norm based data conformity cleaning method produces a clean spectrum, where the AoA of the beacon is clearly distinguishable.

V. Conclusions

We presented a novel data cleaning method for angle-of-arrival estimation based on data conformity evaluation. The proposed method utilizes an iteratively refined L1-norm tensor decomposition algorithm, which measures the conformity of each received tensor entry with respect to the whole tensor dataset. Non-conforming slabs are removed, resulting in a clean dataset for AoA estimation. We show on real data that the proposed method significantly enhances the performance of AoA estimation compared to traditional L2-norm methods.

References

[1] J. Scherer, S. Yahyanejad, S. Hayat, E. Yanmaz, T. Andre, A. Khan, V. Vukadinovic, C. Bettstetter, H. Hellwagner, and B. Rinner, "An autonomous multi-uav system for search and rescue," in *Proc. Workshop on Micro Aerial Vehicle Networks, Systems, and Applications for Civilian Use*, New York, NY, USA, 2015, pp. 33–38.

[2] J. Qi, D. Song, H. Shang, N. Wang, C. Hua, C. Wu, X. Qi, and J. Han, "Search and rescue rotary-wing uav and its application to the lushan ms 7.0 earthquake," *Journal of Field Robotics*, vol. 33, no. 3, pp. 290–321, 2016.

[3] S. Omari, P. Gohl, M. Burri, M. Achtelik, and R. Siegwart, "Visual industrial inspection using aerial robots," in *Proc. Int. Conf. on Applied Robotics for the Power Industry*, Oct 2014.

[4] J. Cacace, A. Finzi, V. Lippiello, G. Loianno, and D. Sanzone, "Aerial service vehicles for industrial inspection: task decomposition and plan execution," *Applied Intelligence*, vol. 42, no. 1, pp. 49–62, 2015.

[5] P. Tokekar, J. Vander Hook, D. Mulla, and V. Isler, "Sensor planning for a symbiotic uav and ugv system for precision agriculture," in *Proc. IEEE Int. Conf. on Intelligent Robots and Systems*, Nov 2013, pp. 5321–5326.

[6] Y. Lu, D. Macias, Z. S. Dean, N. R. Kreger, and P. K. Wong*, "A uav-mounted whole cell biosensor system for environmental monitoring applications," *IEEE Trans. Nanobiosci.*, vol. 14, no. 8, pp. 811–817, Dec 2015.

[7] N. Patwari, J. N. Ash, S. Kyperountas, A. O. Hero, R. L. Moses, and N. S. Correal, "Locating the nodes: cooperative localization in wireless sensor networks," *IEEE Signal Processing Magazine*, vol. 22, no. 4, pp. 54–69, Jul 2005.

[8] M. Haardt, F. Roemer, and G. Del Galdo, "Higher-order svd-based subspace estimation to improve the parameter estimation accuracy in multidimensional harmonic retrieval problems," *IEEE Trans. Signal Processing*, vol. 56, no. 7, pp. 3198–3213, July 2008.

[9] O. Tekdas and V. Isler, "Sensor placement for triangulation-based localization," *IEEE Trans. on Automation Science and Engineering*, vol. 7, no. 3, pp. 681–685, Jul. 2010.

[10] H. Bayram, J. V. Hook, and V. Isler, "Gathering bearing data for target localization," *IEEE Robotics and Automation Letters*, vol. 1, no. 1, pp. 369–374, Jan 2016.

[11] H. Durrant-Whyte and T. Bailey, "Simultaneous localization and mapping: part i," *IEEE Robotics Automation Magazine*, vol. 13, no. 2, pp. 99–110, Jun 2006.

[12] T. Bailey and H. Durrant-Whyte, "Simultaneous localization and mapping (slam): part ii," *IEEE Robotics Automation Magazine*, vol. 13, no. 3, pp. 108–117, Sep. 2006.

[13] J. Wang, M. Garratt, A. Lambert, J. J. Wang, S. Han, and D. Sinclair, "Integration of GPS/INS/vision sensors to navigate unmanned aerial vehicles," *The International Archives of the Photogrammetry, Remote Sensing and Spatial Information Sciences*, vol. 37, no. part B1, pp. 963–969, 2008.

[14] N. Tsagkarakis, P. P. Markopoulos, and D. A. Pados, "Direction finding by complex L1-principal-component analysis," in *IEEE Int. Workshop on Signal Processing Advances in Wireless Communications*, Jun 2015, pp. 475–479.

[15] N. Tsagkarakis, P. P. Markopoulos, G. Sklivanitis, and D. A. Pados, "L1-norm principal-component analysis of complex data," *IEEE Trans. Signal Processing*, vol. 66, no. 12, pp. 3256–3267, June 2018.

[16] K. Tountas, D. A. Pados, and M. J. Medley, "Conformity evaluation and L_1-norm principal-component analysis of tensor data," in *SPIE Big Data: Learning, Analytics, and Applications Conf., SPIE Defense and Commercial Sensing*, Baltimore, MD, Apr. 2019.

[17] P. P. Markopoulos, G. N. Karystinos, and D. A. Pados, "Optimal algorithms for L_1-subspace signal processing," *IEEE Trans. Signal Processing*, vol. 62, no. 19, pp. 5046–5058, Oct 2014.

[18] P. P. Markopoulos, S. Kundu, S. Chamadia, and D. A. Pados, "Efficient L1-norm principal-component analysis via bit flipping," *IEEE Trans. Signal Processing*, vol. 65, no. 16, pp. 4252–4264, Aug. 2017.

[19] Y. Liu and D. A. Pados, "Conformity evaluation of data samples by L_1-norm principal component analysis," in *Proc. SPIE, Compressive Sensing VII: From Diverse Modalities to Big Data Analytics*, vol. 10658, Orlando, FL, Apr. 2018, pp. 1–9.